
Equivariant Networks for Porous Crystalline Materials

Marko Petković*

Eindhoven University of Technology
EAISI
m.petkovic1@tue.nl

Pabloe Romero Marimon*

Eindhoven University of Technology
p.romero.marimon@student.tue.nl

Vlado Menkovski*

Eindhoven University of Technology
EAISI
v.menkovski@tue.nl

Sofia Calero*

Eindhoven University of Technology
EAISI
s.calero@tue.nl

Abstract

Porous crystalline materials have the potential to play a key role in developing solutions for molecular storage, gas separation and carbon adsorption. For these solutions, we need to develop new materials with specific properties. Estimating the properties of such porous materials involves first principle simulation using classical molecular simulations. The computational complexity of these methods can be a barrier to high throughput screening of the potential materials as the space of possible materials is vast. Data-driven methods, specifically machine learning methods based on deep neural networks offer a significant opportunity to significantly scale the simulation of the behavior of these materials. However, to effectively achieve this the Deep Learning models need to utilize the symmetries present in the crystals. Crystals pose specific symmetries that are present in their space group. Existing methods for crystal property prediction either have symmetry constraints that are too restrictive or only incorporate symmetries between unit cells. In addition, these models do not explicitly model the porous structure of the crystal. In this paper, we develop a model which incorporates the symmetries of the unit cell of a crystal in its architecture and explicitly models the porous structure. We evaluate our model by predicting the heat of adsorption of CO₂ for different configurations of the Mordenite and ZSM-5 zeolites. Our results confirm that our method performs better than existing methods for crystal property prediction and that the inclusion of pores results in a more efficient model.

1 Introduction

Deep Learning has shown to be of great use in materials science, in tasks like property prediction and high-throughput screening of potential materials [1]. In these workflows, many materials are first simulated using first principles methods, such as Density Functional Theory (DFT) and classical simulation, such as Molecular Dynamics (MD), to find candidate materials to synthesize. However, these simulations are often computationally expensive and can take days or weeks to simulate a single new material. With Deep Learning, it is possible to accelerate the process of finding suitable materials, by developing data-driven surrogate models. These models scale significantly better than first principle simulators and allow for efficient search of the space of potential candidates [2]. Graph Neural Network (GNN) architectures are commonly used for modeling molecules and materials [3] as these objects can effectively be represented as a graph. However, general-purpose GNNs are too restrictive with regard to symmetries they incorporate or only incorporate part of the symmetries present in crystal structures.

*Equal contribution.

To overcome these limitations, for crystalline materials, multiple GNN architectures have recently been proposed [4–7] that accurately predict the properties of materials. These methods are specific extensions of general-purpose GNN that preserve the geometric structure of the crystal in their data representation. Nevertheless, none of the proposed models explicitly encode any information regarding pores or do not make use of all the symmetries present in the crystal material representation. We hypothesize that model architectures that do not explicitly model the porous structure of porous materials will struggle to infer the relevance of atom arrangements around pores for different properties.

Zeolites are a type of porous, crystalline materials of particular interest, as they are easily synthesizable [8]. They are used in applications such as ion exchange and gas separation and are a potential method for carbon capture [9]. The crystal structure of zeolites entirely consists of TO_4 tetrahedra. In these tetrahedra, the T-atoms can either be aluminium or silicon, and both have different influences on the properties of the material. All four corners of the tetrahedra are shared, which results in a porous material. In Figure 1a, the porous structure of the Mordenite zeolite can be seen. The ability to capture CO_2 of a zeolite can be measured by its heat of adsorption in kJ/mol and is calculated using Equation 1. Here, ΔU is the difference in internal energy before and after adsorption, R is the universal gas constant, and T is the temperature. The heat of adsorption can be influenced by the structure of the different types of zeolites, as well as the amount and distribution of aluminium atoms in the framework [10–12].

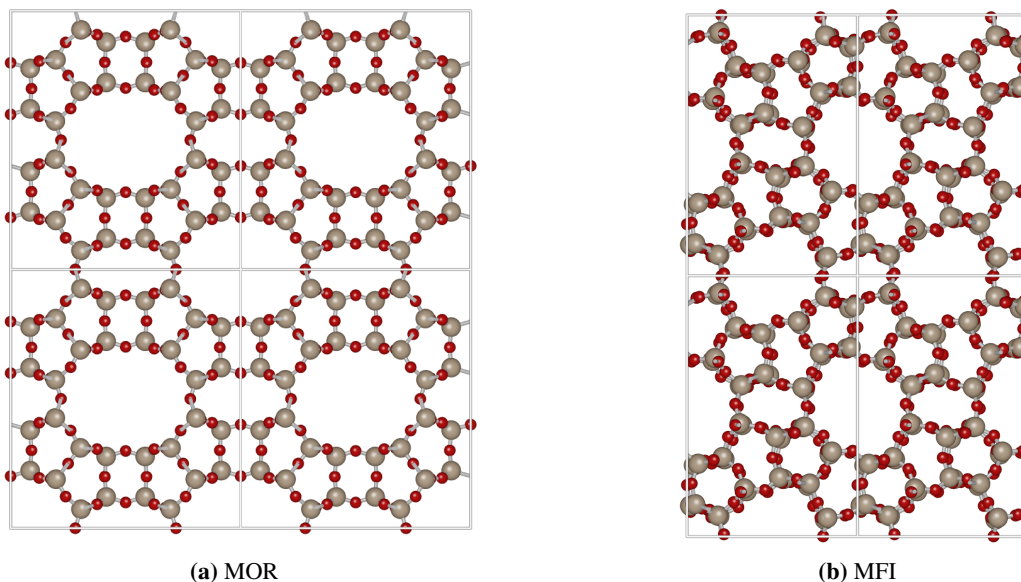


Figure 1: Four unit cells of all silica MOR and MFI viewed along the z-axis and y-axis respectively. Images were generated using iRASPA [13].

Due to the difference in charge between aluminium and silicon atoms, it is necessary to balance the charge of the zeolite when aluminium atoms are present in a framework. To achieve this, cations such as sodium are inserted in the crystal structure. Since the cations themselves are positively charged, they additionally attract CO_2 through Coulombic (electrostatic) forces, thus increasing the ability of the material to adsorb CO_2 . However, while the cations increase the adsorption strength, they also occupy physical space in the pores of the material. When there are multiple sodium cations inside a pore, they can restrict CO_2 from entering it. As a result, the adsorption capacity of the material decreases. It is unclear which distributions of aluminium and silicon in different zeolites are optimal to maximize the heat of adsorption.

$$-\Delta H = \Delta U - RT \quad (1)$$

In this paper, we propose a novel GNN architecture that exploits information regarding the porous structure, as well as the symmetry of these materials, using parameter-sharing based on their space groups. This model allows us to effectively model the properties of porous crystalline materials.

We empirically validate our approach by modeling the heat of adsorption of CO₂ for the Mordenite (MOR) and the ZSM-5 (MFI) zeolite. Our contributions are threefold: 1) We adapt the Equivariant Crystal Networks (ECN) architecture from [5] to be equivariant with respect to the symmetry group of the unit cell. 2) We additionally extend this architecture to explicitly model pores and show how this modification improves property prediction performance. 3) We introduce a new dataset containing different configurations of aluminium and silicon for the MOR and MFI zeolites, along with the CO₂ heat of adsorption values for the different configurations.

2 Related Work

2.1 Machine Learning Methods for Crystals

Due to the success of different GNN architectures in modeling molecules, similar GNN architectures have been proposed for predicting the properties of material data. Crystal Graph Convolutional Neural Networks (CGCNN) [7] are one of the first GNN architectures for crystals, which also include periodicity in the data representation and are invariant with respect to permutations of atomic indices. They can be seen as an extension of message passing [14] and Graph Convolutional Networks [15]. In the MEGNet architecture [4], CGCNN is extended with a global state, that is used to improve the generalization of the model. Continuous filter convolutions have been introduced in the SchNet architecture [16], which as a result can model the precise relative locations of atoms better when calculating local correlations. SchNet achieves invariance by pooling the final states of each atom. Another approach has been proposed in DimeNet [17], where in addition to the distances between atoms, the network also takes directional information between atoms into account. The network was designed for molecules, and was further extended with DimeNet++ [18], which is faster and more accurate. More recently a new approach has been proposed [5], which proposes a parameter-sharing scheme for message-passing, based on the symmetry group of the crystal lattice. As such, the model gains in expressivity by encoding a part of the crystal symmetries in the model architecture.

2.2 Machine Learning in Porous Materials

Existing ML methods for property prediction often make use of feature engineering, which traditional ML models or shallow neural networks use to predict properties of the material [19, 20]. Another approach made use of the CGCNN architecture [21] and extended it with engineered features [22] to improve performance. In their method, nodes in the graph representation do not correspond to atoms but rather correspond to secondary building units (SBUs), which consist of multiple atoms.

3 Crystal Symmetries

In this section, we briefly summarize crystal symmetries based on [5] and show how we extend these to our case of porous crystalline materials.

3.1 Unit Cell

Zeolites are crystalline materials, meaning that they contain an infinitely repeating pattern in all directions. This repeating pattern can be described by the set of integral combinations of linearly independent lattice basis vectors \mathbf{a}_i :

$$\Lambda = \left\{ \sum_i^3 m_i \mathbf{a}_i \mid m_i \in \mathbb{Z} \right\} \quad (2)$$

The crystal lattice has an associated translation group T_Λ , which captures translational symmetry. A unit cell is a subset of the lattice, which tiles the space of the crystal when translated by lattice vectors and is the minimum repeating pattern of the crystal. The unit cell is defined by the basis vectors as follows:

$$U = \left\{ \sum_i^3 x_i \mathbf{a}_i \mid 0 \leq x_i < 1 \right\} \quad (3)$$

The unit cell of a crystalline material contains a set of atomic positions, which is defined as $S = \{\mathbf{x}_i \mid \mathbf{x}_i \in U\}$, where \mathbf{x}_i is the position of the atom in the unit cell. In addition to the set of atomic positions, we also define the set of pores contained in the unit cell. We define each pore using the atoms directly surrounding the pore. We represent each pore by the location of its center, as well as its surface area along which diffusion happens in terms of \AA^2 . This results in the following set of pores: $P = \{(\mathbf{x}_{p_i}, \text{area}(p_i)) \mid p_i \in U\}$, where p_i is the pore and \mathbf{x}_{p_i} is the centre of the pore.

3.2 Space Groups

In crystalline materials, there are often multiple symmetries present inside the unit cell, defined by a space group G . The space group G is the set of isometries that maps the crystal structure onto itself. Each element of the space group can be expressed as a linear transformation \mathbf{W} and a translation \mathbf{t} , represented by a tuple (\mathbf{W}, \mathbf{t}) . When mapping a vector \mathbf{x} using an element of the space group, it is mapped to $\mathbf{W}\mathbf{x} + \mathbf{t}$.

Inside a unit cell, every element of the space group G maps the atomic positions and the positions of the pores in the unit cell onto itself. While the type of atom at a certain position in the unit cell might change as a result of a transformation, the material remains the same. Therefore, each group action g of the space group can be considered a permutation of the atoms and pores in the unit cell.

3.3 Group Orbits

By applying all the different elements of a space group G to an element, we create the orbit of an element. In case the element is a vector \mathbf{x} , its orbit is the set of vectors that the element can be moved to by the group action. The orbit of \mathbf{x} is defined as follows:

$$G \cdot \mathbf{x} = \{g \cdot \mathbf{x} \mid g \in G\} \quad (4)$$

4 Methods

4.1 Crystal Representation

In our crystal representation, we only consider the set of atoms inside of the unit cell, as the content of a unit cell fully defines the porous structures and symmetry of the material. Each of the atoms in the unit cell is represented by a feature vector \mathbf{a}_i that is a one-hot encoding of the atom type. Next to this, we represent each pore inside the unit cell with a feature vector \mathbf{p}_i , which contains the surface area of the pore, as well as the number of atoms surrounding that pore.

To represent the topology of the atoms and pores we construct a graph, where each atom is represented with a node. When the crystal contains clearly defined covalent bonds these can be used to represent edges in the graph, like in the case of zeolites. Otherwise, edges could be drawn between atoms that share a Voronoi face and are sufficiently close to each other [23], or between all atoms within a certain distance of each other [16].

Finally, to include the pores in the graph representation, we add additional edges between the pore nodes and each atom on the boundary of the pore. By including these nodes, all atoms around the same pore are reachable from each other at most in two steps. Without pore nodes, this number could have been significantly larger, particularly for crystals with larger pores.

The notion of a pore has a certain analogy to the global feature vector introduced in MEGNet [4]. However, our approach is distributed in the geometry of the crystal which in turn allows the GNN-based model to learn locally distributed features, which is a more parameter-efficient solution.

Based on [16], we make use of radial basis functions to encode the distance between two neighboring nodes in the graph. We calculate the edge embedding \mathbf{e}_{ij} as in Equation 5, where γ and μ are hyperparameters.

$$\mathbf{e}_{ij} = \exp(-\gamma(\|\mathbf{x}_i - \mathbf{x}_j\| - \mu)^2) \quad (5)$$

When calculating the distance between two atoms, we respect the periodic boundary conditions set by the unit cell by using the minimum image convention. Thus, we treat the opposite boundaries as a single boundary and consider the atoms and pores as neighbors and therefore sharing an edge.

Since we are creating and developing a network architecture to predict properties based on the silicon and aluminium configuration in zeolites, we do not explicitly encode the oxygen atoms as nodes, as

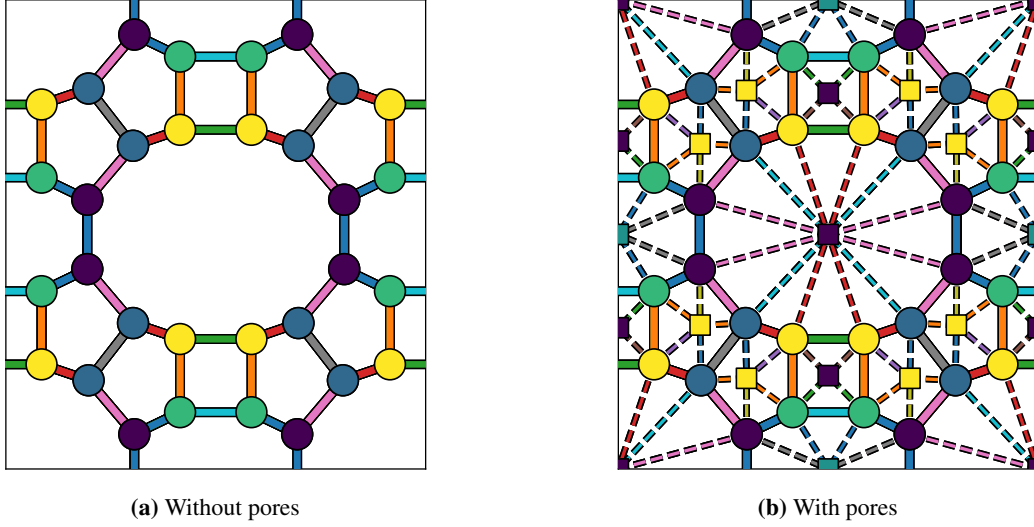


Figure 2: Weight sharing scheme for MOR, viewed along the z-axis. Nodes/edges that are the same color share parameters in their node/edge update functions. Dashed edges are between atoms (circle) and pores (squares), while solid edges are between atoms. Note that in some edges 2 different sets of parameters are used, as in some cases sending a message from node i to j is not symmetric to sending a message from node j to i .

only the atoms placed in the T-sites of each TO_4 tetrahedron can change, while the oxygen atoms always remain in the same position.

4.2 Equivariant Message Passing

Since the space group acts as a permutation on the atoms and pores in the unit cell, we can describe the action of a group element using Equation 6. Here, π_g^{a} and π_g^{p} are the permutations of the atoms and pores as a result of group action g .

$$\left(g\mathbf{a}_i = \mathbf{a}_{\pi_g^{\text{a}}(i)} \wedge g\mathbf{p}_j = \mathbf{p}_{\pi_g^{\text{p}}(j)} \right) \forall g \in G \quad (6)$$

As we model different configurations of the same crystal structure using our architecture, we need to create a model which is equivariant to G . The model we define is based on the message passing framework [14], which we extend by defining parameter-sharing patterns [24] for the edge and node update functions.

First, we will define how a parameter-sharing pattern for a graph is calculated. Following [5], we define the parameter-sharing pattern as the colored bipartite graph $\Omega \equiv (\mathbb{N}, \alpha, \beta)$. Here, \mathbb{N} is the set of input atoms and pores, α is the edge color function ($\alpha : \mathbb{N} \times \mathbb{N} \rightarrow \{1, \dots, C_e\}$) and β is the node color function ($\beta : \mathbb{N} \rightarrow \{1, \dots, C_h\}$). For the functions, α and β , C_e and C_h are the amounts of unique edge colors and node colors respectively. As shown in Equations 7 and 8, the color functions take the same value if two edges or atoms/pores lie on each other's orbit.

$$\alpha(i, j) = \alpha(k, l) \iff (k, l) \in G \cdot (i, j) \quad (7)$$

$$\beta(i) = \beta(j) \iff j \in G \cdot i \quad (8)$$

When introducing a parameter-sharing pattern based on the edge and node coloring function, we are effectively introducing an additional edge (node) update function for each unique edge (node) in the graph representation of the crystal. As such, the model architecture is equivariant to the space group of the crystal, following Claim 6.1 from [5]. In Figure 2, an example of what the parameter-sharing pattern for MOR looks like can be found, where nodes and edges are colored according to Equations 7 and 8. The message passing operation equivariant to the space group is defined in Equations 9-11, where \mathbf{h}_i is the node embedding. In Appendix A the set of equations can be found which additionally differentiates between atom and pore nodes.

Since the space group does not change as a result of including the pore nodes in the graph, the colors of the edges between atoms and the colors of the atoms themselves remain the same. As a result, the

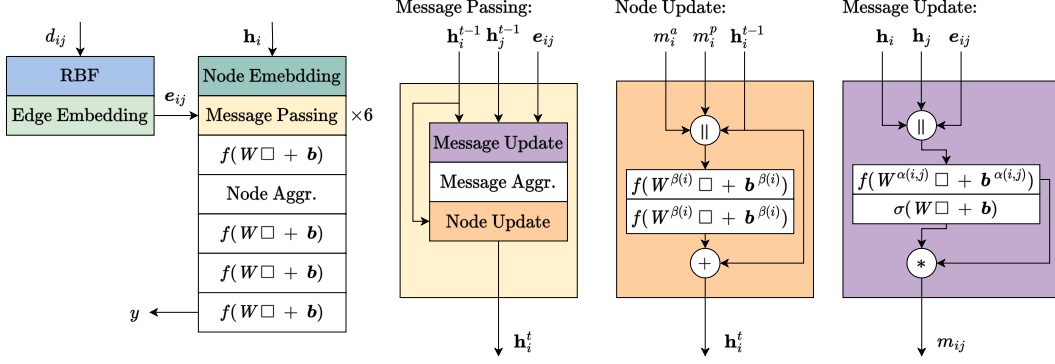


Figure 3: Overview of the network architecture with pores. The \square and \parallel denote the layer’s input and concatenation respectively. The $+$ and $*$ denote elementwise summation and multiplication. \mathbf{h}_i represents the embedding of node i (which can be an atom or a pore), while d_{ij} represents the distance between nodes i and j . f represents the leaky ReLU activation function, while σ is the sigmoid activation function. Note that in the node update function, pore nodes (or all nodes in the architecture without pores) do not receive messages from pores (m_i^p). In addition, the node embedding operation is different for atom and pore nodes.

model remains equivariant to the space group of the crystal. However, since different types of crystals have different amounts of atoms and/or different space groups, we cannot share the parameters of message-passing operations between crystals, meaning that each crystal needs its own unique model.

$$\mathbf{m}_{ij} = \phi_e^{\alpha(i,j)}(\mathbf{h}_i^t, \mathbf{h}_j^t, \mathbf{e}_{ij}), \quad (9)$$

$$\mathbf{m}_i = \frac{1}{|N_i|} \sum_{j \in N_i} \mathbf{m}_{ij}, \quad (10)$$

$$\mathbf{h}_i^{t+1} = \phi_h^{\beta(i)}(\mathbf{h}_i^t, \mathbf{m}_i^h), \quad (11)$$

5 Experiments

5.1 Network Architecture

In Figure 3, an overview of the model architecture is presented. First, the edges are embedded by applying Equation 5 to their distance (d_{ij}), which is followed by a fully connected layer. Simultaneously, both atoms and pores are embedded using two different fully connected layers, as atoms have only one feature while pores have two. In the message update function, the embeddings of the sending and receiving node and the edge embedding are concatenated, which is followed by a fully connected layer that shares weights according to Equation 7. Each message also receives a weighting factor, calculated by the fully connected layer following the equivariant layer.

The message aggregation step depends on the node type. As a result of including pore nodes in the graph, we distinguish between two types of messages, depending on whether they are sent from an atom or a pore. To allow the model to distinguish between the origin of the messages, we separately aggregate messages sent from pores (m_i^p) and atoms (m_i^a) in the node update function. When using the version of the model without pores, all messages are aggregated together at the node update step, since all incoming messages are from atoms. Following the concatenation of the different messages and the node embedding, we apply 2 linear layers. The node update block also contains a skip connection [25] from the previous node embedding to the new node embedding.

Following multiple message-passing steps, the node features are aggregated, and a 3-layer MLP is applied to obtain the final prediction. We use sum aggregation in the node aggregation step. In the model with pores, we only aggregate the pore node features. This way, we implicitly force the model to learn how much each pore contributes to the adsorption capacity.

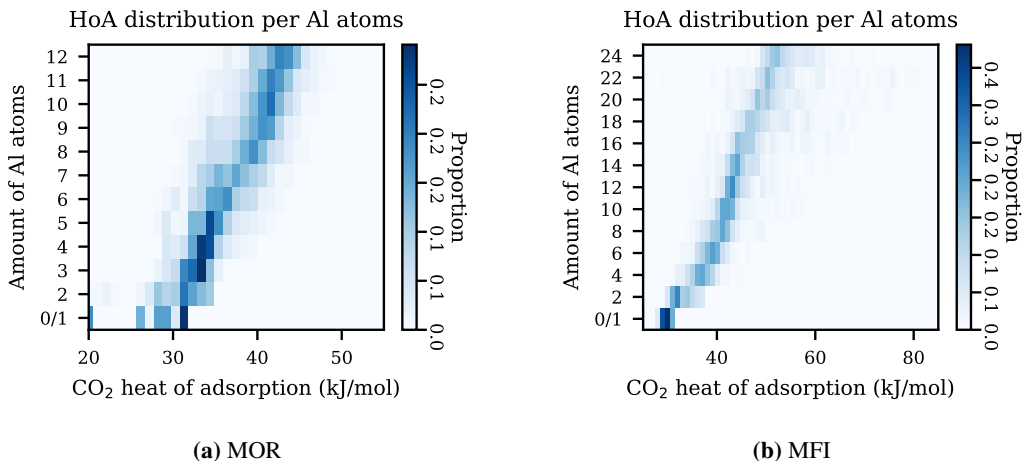


Figure 4: Heat of Adsorption distributions per amount of aluminium atoms for MOR and MFI. As we are training the model on a single crystal structure at a time, it suffices to keep the architecture relatively simple. We perform 6 message passing steps, with an embedding size for both edges and atoms (pores) of 8. Then, we process each atom (pore) with an MLP with an output size of 24. Following this, sum pooling is used to perform an invariant aggregation, which is followed by a 3-layer MLP to make predictions. Our model implementation is based on [5] and uses the PyTorch [26] and PyTorch scatter [27] packages as well as the AutoEquiv library [28].

5.2 Data Generation

To generate a dataset with porous, crystalline materials, we made use of the Mordenite and ZSM-5 zeolite frameworks. MOR is a simpler zeolite, containing 48 T-atoms, where adsorbates mainly diffuse along the z-axis. MFI is a more complex zeolite, which contains 96 T-atoms. It has multiple intersecting pores, and adsorbates can diffuse along both the x-axis and y-axis. As a result, the adsorption capacity between two configurations with an equal amount of aluminium atoms can vary greatly. More information on the datasets and structures can be found in Appendix B.

We generated multiple MOR and MFI frameworks with varying aluminum and silicon distributions, and carried out simulations to calculate the corresponding CO_2 heat of adsorption for each configuration. For generating the structures, the Zeoran program was used [29] and atom coordinates were taken from [30]. For MOR, 4992 structures were generated, where each structure contains up to 12 aluminium atoms. For MFI, 3296 structures were generated with up to 24 aluminium atoms. The amount of aluminium atoms was chosen such that they roughly match what is possible in practice. The program makes use of four different algorithms, which places aluminium atoms in either random positions, chains, clusters or homogeneously throughout the zeolite framework. To calculate the CO_2 heat of adsorption Grand-Canonical Monte Carlo simulations were carried out using the Widom Particle Insertion method [31], performed with the RASPA software [32]. Frameworks were considered rigid and the force field parameters for the interactions between the zeolite and the adsorbate were taken from [33]. The force field for carbon dioxide was taken from [34].

In Figure 4, the distribution of the heat of adsorption in both datasets is shown. While there is a strong correlation between the amount of aluminium atoms and the heat of adsorption, there is still significant variance in the heat of adsorption for each amount of aluminium substitutions (Figure 4). As such, a more complex model is necessary to understand the influence of different configurations on the heat of adsorption.

5.3 Model Evaluation

To evaluate the predictive performance and the ability of our models to generalize, we performed two experiments. In the first experiment, we made an uninformed, random assignment of samples to the training (90%) and testing set (10%). In the second experiment, we investigated the models capability to generalize, by testing the model on configurations with 12 aluminium atoms for MOR (4562 training and 430 testing structures) and with 22 and 24 aluminium atoms for MFI (2941 training and 355 testing structures). Note that in both cases roughly 10% of the dataset is used for testing. In the

Table 1: Performance of different model architectures on CO₂ heat of adsorption prediction for the MOR and MFI datasets for the random train/test split.

	MOR		MFI	
	MAE	MSE	MAE	MSE
Linear Regression	1.945	6.583	3.045	20.097
DimeNet++	1.696 ± 0.090	5.132 ± 0.460	2.862 ± 0.027	19.344 ± 0.472
CGCNN	1.673 ± 0.087	4.822 ± 0.422	2.770 ± 0.060	18.545 ± 0.842
MEGNet	1.529 ± 0.077	4.238 ± 0.433	2.733 ± 0.063	19.024 ± 1.068
SchNet	1.046 ± 0.015	2.041 ± 0.084	2.357 ± 0.052	10.953 ± 0.471
Ours (without pores)	1.050 ± 0.049	2.805 ± 0.312	2.009 ± 0.060	8.819 ± 0.416
Ours (with pores)	0.877 ± 0.018	1.488 ± 0.050	1.996 ± 0.049	9.012 ± 0.344

Table 2: Performance of different model architectures on CO₂ heat of adsorption prediction for the MOR and MFI datasets for the generalization train/test split.

	MOR		MFI	
	MAE	MSE	MAE	MSE
Linear Regression	1.862	6.119	4.731	42.979
DimeNet++	1.751 ± 0.048	5.247 ± 0.230	3.965 ± 0.023	40.054 ± 0.788
CGCNN	1.681 ± 0.081	4.967 ± 0.419	4.144 ± 0.109	40.745 ± 1.617
MEGNet	1.520 ± 0.053	4.269 ± 0.270	4.243 ± 0.231	41.448 ± 2.783
SchNet	1.148 ± 0.049	2.332 ± 0.154	3.728 ± 0.283	26.419 ± 2.984
Ours (without pores)	1.269 ± 0.094	2.805 ± 0.312	3.309 ± 0.145	21.488 ± 1.588
Ours (with pores)	1.042 ± 0.037	1.981 ± 0.116	2.864 ± 0.109	17.742 ± 0.792

results section we will mainly focus on the random split, as in practice structures with any amount of aluminum atoms can be generated for training.

We compare the performance of our model with and without pores to different baselines [7, 16, 23], as well as a version of DimeNet++ [18] adapted to take the periodicity of crystals into account. To understand how well the different networks learn the influence of the distribution of aluminium atoms, we also compare the results to a linear regression based on the amount of aluminium atoms. To compare the baselines with our model, we make them with the same level of complexity as our model, using 6 message passing/interaction steps, hidden sizes of 8, and a final MLP with 24 nodes.

Since predicting the heat of adsorption is a regression task, we made use of the Huber loss function when training. We used the AdamW optimizer [35] with a learning rate of 0.001, and trained each model for 200 epochs. We report the mean-absolute error (MAE) and mean-squared error (MSE). To obtain confidence bounds for the errors, we trained each model 10 times with random initializations of their weights. The code for the model implementations and the zeolite dataset are available on <https://github.com/marko-petkovic/porousequivariantnetworks>.

As can be seen in Tables 1 and 2, our model with pores obtains the best results on both evaluation tasks. Furthermore, we note that in both cases our model without pores and SchNet achieve comparable results. The other baselines only offer a small improvement over linear regression. We speculate that this behaviour is caused by the spatial features of the zeolites (pores) not explicitly being encoded in the graph representation. As such, it might be hard for them to learn the relationship between the distribution of aluminium atoms and the heat of adsorption. On the other hand, our models and SchNet have the ability to exploit symmetries and spatial features in the unit cell, which could explain their better performance. We also note that SchNet performs significantly worse than our models on MFI, which may be explained by the higher complexity of the material.

In Figure 6, we plotted the true against the predicted heat of adsorption values for our best model with pores on the MOR and MFI datasets with the random train/test split. We see that most predictions for both models are accurate. For higher heat of adsorption values, the model for MFI performs slightly worse. This may be due to an insufficient amount of training examples present with a high heat of adsorption.

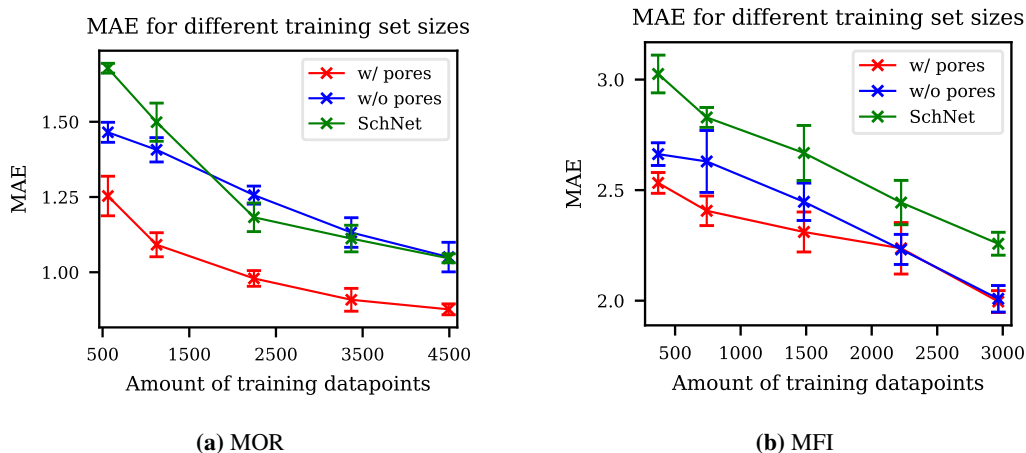


Figure 5: Data efficiency (MAE on test set) with different amounts of training data (random split).

In addition, we carried out experiments to compare the data efficiency of our model with pores, without pores and SchNet. Here, we trained each model using different fractions ($\frac{1}{8}$, $\frac{1}{4}$, $\frac{1}{2}$, $\frac{3}{4}$ and 1) of the training set, and evaluated them on the same testing set. In Figure 5a, we see that our model with pores has a significantly better data efficiency than our model without pores and SchNet for MOR. In the case of MFI (Figure 5b), we see that both our models have a better data efficiency than SchNet, with our model with pores performing slightly better for low amounts of training data. In Appendix C, additional results can be found.

6 Discussion

We have proposed a new type of network which can exploit both symmetries inside the unit cell as well as the structure of porous crystalline materials. Our method achieved excellent performance on the CO₂ heat of adsorption prediction task, and has also shown a better data efficiency. This class of models has a significant potential to accelerate the high throughput screening of porous materials, by quickly narrowing the search space for candidate materials. A drawback of our method is the inability to train the model on multiple crystals at the same time. A potential direction for future research could be to base the parameter-sharing on Composite Building Units (CBUs) of zeolites or metal organic frameworks, as multiple structures share the same CBUs. This way, increased expressivity of the parameter-sharing idea is retained, while the model can generalize beyond a single type of crystal.

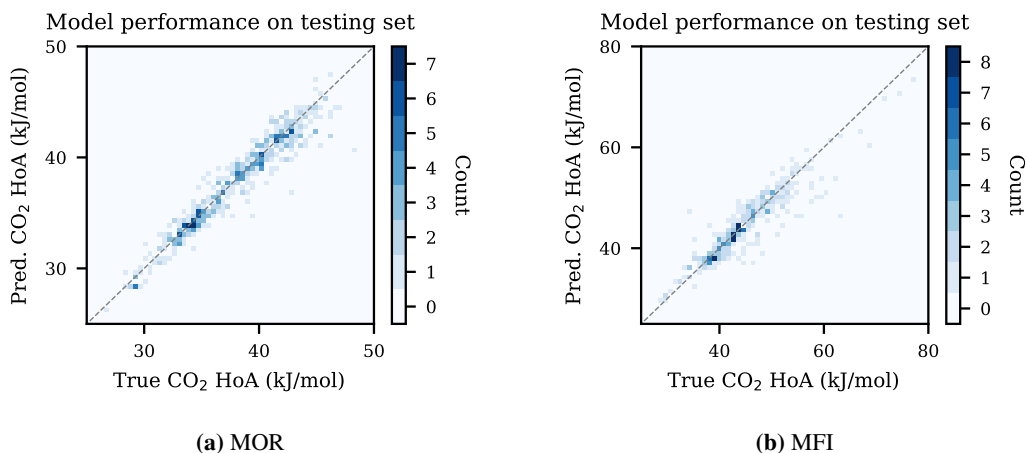


Figure 6: Predicted heat of adsorption plotted against the true heat of adsorption for the random train/test split. The best performing model with pores on the test set was used for MOR and MFI.

References

- [1] Kamal Choudhary, Brian DeCost, Chi Chen, Anubhav Jain, Francesca Tavazza, Ryan Cohn, Cheol Woo Park, Alok Choudhary, Ankit Agrawal, Simon JL Billinge, et al. Recent advances and applications of deep learning methods in materials science. *npj Computational Materials*, 8(1):59, 2022. 1
- [2] Helge S Stein and John M Gregoire. Progress and prospects for accelerating materials science with automated and autonomous workflows. *Chemical science*, 10(42):9640–9649, 2019. 1
- [3] Patrick Reiser, Marlen Neubert, André Eberhard, Luca Torresi, Chen Zhou, Chen Shao, Housam Metni, Clint van Hoesel, Henrik Schopmans, Timo Sommer, et al. Graph neural networks for materials science and chemistry. *Communications Materials*, 3(1):93, 2022. 1
- [4] Chi Chen, Weike Ye, Yunxing Zuo, Chen Zheng, and Shyue Ping Ong. Graph networks as a universal machine learning framework for molecules and crystals. *Chemistry of Materials*, 31(9):3564–3572, 2019. 2, 3, 4
- [5] Sékou-Oumar Kaba and Siamak Ravanbakhsh. Equivariant networks for crystal structures. In *Advances in Neural Information Processing Systems*, 2022. 3, 5, 7
- [6] Kristof T Schütt, Huziel E Saucedo, P-J Kindermans, Alexandre Tkatchenko, and K-R Müller. Schnet—a deep learning architecture for molecules and materials. *The Journal of Chemical Physics*, 148(24):241722, 2018.
- [7] Tian Xie and Jeffrey C Grossman. Crystal graph convolutional neural networks for an accurate and interpretable prediction of material properties. *Physical review letters*, 120(14):145301, 2018. 2, 3, 8
- [8] Abdul Khaleque, Md Masruck Alam, Mozammel Hoque, Shuvodip Mondal, Jahid Bin Haider, Bentuo Xu, MAH Jahir, Aneek Krishna Karmakar, JL Zhou, Mohammad Boshir Ahmed, et al. Zeolite synthesis from low-cost materials and environmental applications: A review. *Environmental Advances*, 2:100019, 2020. 2
- [9] Gregor Sneddon, Alex Greenaway, and Humphrey HP Yiu. The potential applications of nanoporous materials for the adsorption, separation, and catalytic conversion of carbon dioxide. *Advanced Energy Materials*, 4(10):1301873, 2014. 2
- [10] Hyun June Choi, Donghui Jo, and Suk Bong Hong. Effect of framework si/al ratio on the adsorption mechanism of co2 on small-pore zeolites: Ii. merlinoite. *Chemical Engineering Journal*, 446:137100, 2022. 2
- [11] Hojatollah Moradi, Hedayat Azizpour, Hossein Bahmanyar, Nariman Rezamandi, and Payam Zahedi. Effect of si/al ratio in the faujasite structure on adsorption of methane and nitrogen: a molecular dynamics study. *Chemical Engineering & Technology*, 44(7):1221–1226, 2021.
- [12] Chi-Ta Yang, Amber Janda, Alexis T Bell, and Li-Chiang Lin. Atomistic investigations of the effects of si/al ratio and al distribution on the adsorption selectivity of n-alkanes in brønsted-acid zeolites. *The Journal of Physical Chemistry C*, 122(17):9397–9410, 2018. 2
- [13] David Dubbeldam, Sofia Calero, and Thijs JH Vlugt. iraspa: Gpu-accelerated visualization software for materials scientists. *Molecular Simulation*, 44(8):653–676, 2018. 2
- [14] Justin Gilmer, Samuel S Schoenholz, Patrick F Riley, Oriol Vinyals, and George E Dahl. Neural message passing for quantum chemistry. In *International conference on machine learning*, pages 1263–1272. PMLR, 2017. 3, 5
- [15] Thomas N Kipf and Max Welling. Semi-supervised classification with graph convolutional networks. *arXiv preprint arXiv:1609.02907*, 2016. 3
- [16] Kristof Schütt, Pieter-Jan Kindermans, Huziel Enoc Saucedo Felix, Stefan Chmiela, Alexandre Tkatchenko, and Klaus-Robert Müller. Schnet: A continuous-filter convolutional neural network for modeling quantum interactions. *Advances in neural information processing systems*, 30, 2017. 3, 4, 8
- [17] Johannes Gasteiger, Janek Groß, and Stephan Günnemann. Directional message passing for molecular graphs. In *International Conference on Learning Representations (ICLR)*, 2020. 3
- [18] Johannes Gasteiger, Shankari Giri, Johannes T. Margraf, and Stephan Günnemann. Fast and uncertainty-aware directional message passing for non-equilibrium molecules. In *Machine Learning for Molecules Workshop, NeurIPS*, 2020. 3, 8

- [19] Kevin Maik Jablonka, Daniele Ongari, Seyed Mohamad Moosavi, and Berend Smit. Big-data science in porous materials: materials genomics and machine learning. *Chemical reviews*, 120(16):8066–8129, 2020. 3
- [20] Chi Zhang, Yunchao Xie, Chen Xie, Hongxing Dong, Long Zhang, and Jian Lin. Accelerated discovery of porous materials for carbon capture by machine learning: A review. *MRS Bulletin*, 47(4):432–439, 2022. 3
- [21] Ruihan Wang, Yeshuang Zhong, Leming Bi, Mingli Yang, and Dingguo Xu. Accelerating discovery of metal–organic frameworks for methane adsorption with hierarchical screening and deep learning. *ACS Applied Materials & Interfaces*, 12(47):52797–52807, 2020. 3
- [22] Ruihan Wang, Yurong Zou, Chunchun Zhang, Xin Wang, Mingli Yang, and Dingguo Xu. Combining crystal graphs and domain knowledge in machine learning to predict metal-organic frameworks performance in methane adsorption. *Microporous and Mesoporous Materials*, 331:111666, 2022. 3
- [23] Olexandr Isayev, Corey Oses, Cormac Toher, Eric Gossett, Stefano Curtarolo, and Alexander Tropsha. Universal fragment descriptors for predicting properties of inorganic crystals. *Nature communications*, 8(1):15679, 2017. 4, 8
- [24] Siamak Ravanbakhsh, Jeff Schneider, and Barnabas Poczos. Equivariance through parameter-sharing. In *International conference on machine learning*, pages 2892–2901. PMLR, 2017. 5
- [25] Kaiming He, Xiangyu Zhang, Shaoqing Ren, and Jian Sun. Deep residual learning for image recognition. In *Proceedings of the IEEE conference on computer vision and pattern recognition*, pages 770–778, 2016. 6
- [26] Adam Paszke, Sam Gross, Francisco Massa, Adam Lerer, James Bradbury, Gregory Chanan, Trevor Killeen, Zeming Lin, Natalia Gimelshein, Luca Antiga, et al. Pytorch: An imperative style, high-performance deep learning library. *Advances in neural information processing systems*, 32, 2019. 7
- [27] Matthias Fey. Pytorch scatter, 2023. 7
- [28] Mehran Shakerinava. Autoequiv, 2 2021. URL <https://github.com/mshakerinava/AutoEquiv>. 7
- [29] Pablo Romero-Marimon, Juan José’ Gutiérrez-Sevillano, and Sofia Calero. Adsorption of carbon dioxide in non-löwenstein zeolites. *Chemistry of Materials*, 2023. 7
- [30] Ch Baerlocher, Lynne B McCusker, and David H Olson. *Atlas of zeolite framework types*. Elsevier, 2007. 7
- [31] Ben Widom. Some topics in the theory of fluids. *The Journal of Chemical Physics*, 39(11):2808–2812, 1963. 7
- [32] David Dubbeldam, Sofia Calero, Donald E Ellis, and Randall Q Snurr. Raspa: molecular simulation software for adsorption and diffusion in flexible nanoporous materials. *Molecular Simulation*, 42(2):81–101, 2016. 7
- [33] Almudena Garcia-Sanchez, Conchi O Ania, José B Parra, David Dubbeldam, Thijs JH Vlugt, Rajamani Krishna, and Sofia Calero. Transferable force field for carbon dioxide adsorption in zeolites. *The Journal of Physical Chemistry C*, 113(20):8814–8820, 2009. 7
- [34] Jonathan G Harris and Kwong H Yung. Carbon dioxide’s liquid-vapor coexistence curve and critical properties as predicted by a simple molecular model. *The Journal of Physical Chemistry*, 99(31):12021–12024, 1995. 7
- [35] Ilya Loshchilov and Frank Hutter. Decoupled weight decay regularization. *arXiv preprint arXiv:1711.05101*, 2017. 8

A Space Group Equivariant Message Passing Equations

The full set of equations for message passing with pores can be found in Equations 12 to 19. Unlike in the rest of the paper, \mathbf{h}_i specifically represents atom node embeddings, while \mathbf{p}_i represents pore nodes. Here, we distinguish between messages between atoms (Equation 12), messages sent from atoms to pores (Equation 13) and messages from pores to atoms (Equation 14). Each type of message is aggregated separately (Equations 15-17). The node update function for atoms (Equation 18), takes the previous node embedding, as well as the aggregated messages from pores and atoms as input. The update function for pores (Equation 19) takes only the messages received from atoms in addition to the previous node embedding. Since all inputs in the node update function are concatenated (see Figure 3), the input size is different between the atom and pore update function. As a result, we implemented these two functions separately in the code.

$$\mathbf{m}_{ij}^h = \phi_e^{\alpha(i,j)}(\mathbf{h}_i^t, \mathbf{h}_j^t, \mathbf{e}_{ij}), \quad (12)$$

$$\mathbf{m}_{ij}^k = \phi_e^{\alpha(i,j)}(\mathbf{h}_i^t, \mathbf{p}_j^t, \mathbf{e}_{ij}), \quad (13)$$

$$\mathbf{m}_{ij}^l = \phi_e^{\alpha(i,j)}(\mathbf{p}_i^t, \mathbf{h}_j^t, \mathbf{e}_{ij}), \quad (14)$$

$$\mathbf{m}_i^h = \frac{1}{|N_i^h|} \sum_{j \in N_i^h} \mathbf{m}_{ij}^h, \quad (15)$$

$$\mathbf{m}_i^k = \frac{1}{|N_i^k|} \sum_{j \in N_i^k} \mathbf{m}_{ij}^k, \quad (16)$$

$$\mathbf{m}_i^l = \frac{1}{|N_i^l|} \sum_{j \in N_i^l} \mathbf{m}_{ij}^l, \quad (17)$$

$$\mathbf{h}_i^{t+1} = \phi_{h1}^{\beta(i)}(\mathbf{h}_i^t, \mathbf{m}_i^h, \mathbf{m}_i^k), \quad (18)$$

$$\mathbf{p}_i^{t+1} = \phi_{h2}^{\beta(i)}(\mathbf{p}_i^t, \mathbf{m}_i^l). \quad (19)$$

It should be noted that while we use separate functions for node updates and message updates depending on the type of nodes, the coloring functions α and β (Equation 7 and 8) are applied to the full set of nodes and edges.

B Data

In this work, we analyzed the MOR and MFI zeolites. Here, we will provide additional information about the structure of these zeolites, as well as our dataset.

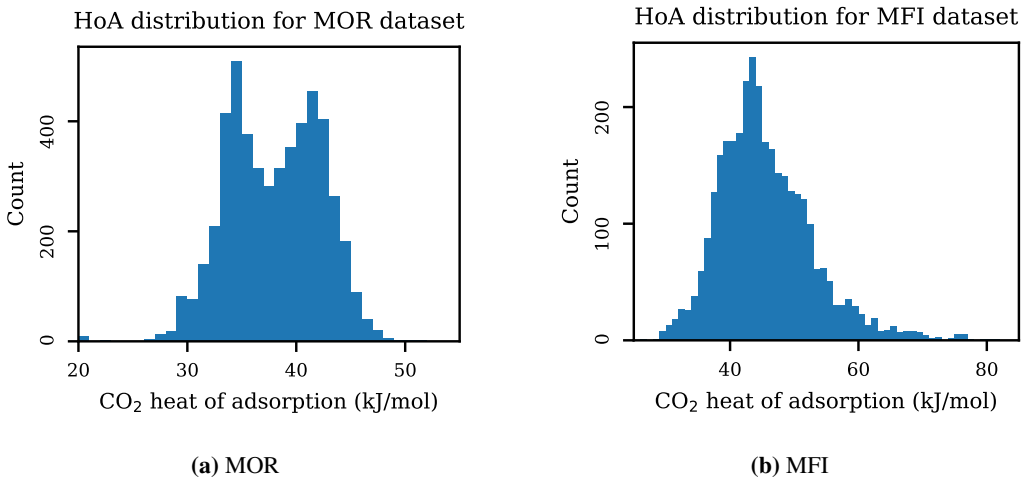


Figure 7: Heat of Adsorption distributions for MOR and MFI.

Table 3: Space group elements for both MOR (Cmcm 63) and MFI (Pnma 62).

(a) Cmcm 63 space group			(b) Pnma 62 space group		
Symmetry operations			Symmetry operations		
x	y	z	x	y	z
-x	-y	-z	-x	-y	-z
-x	y	z	x	1/2-y	z
x	-y	-z	-x	1/2+y	-z
x	-y	1/2+z	1/2-x	-y	1/2+z
-x	-y	1/2+z	1/2+x	y	1/2-z
x	-y	1/2+z	1/2+x	1/2-y	1/2-z
-x	y	1/2-z	1/2-x	1/2+y	1/2+z
x	y	1/2-z			
1/2+x	1/2+y	z			
1/2-x	1/2+y	z			
1/2-x	1/2-y	-z			
1/2+x	1/2-y	-z			
1/2+x	1/2-y	1/2+z			
1/2-x	1/2-y	1/2+z			
1/2-x	1/2+y	1/2-z			
1/2+x	1/2+y	1/2-z			

B.1 MOR

A single unit cell of the MOR zeolite framework contain 48 T-atoms (Al/Si), as well as 96 oxygen atoms. The crystal lattice of MOR is orthorhombic, meaning that all base vectors (a, b, c) are distinct, while they intersect at 90° angles. The lengths of the base vectors are 18.1\AA , 20.5\AA and 7.5\AA respectively. The space group of MOR is Cmcm 63, which contains the operations presented in Table 3a. As a result, there are 4 unique positions (T-sites), in the MOR zeolite, of which two have a site multiplicity of 16, and two have a site multiplicity of 8. Note that the operations are applied to fractional coordinates in the unit cell.

B.2 MFI

MFI has a bigger unit cell, which contains 96 T-atoms (Al/Si) and 192 oxygen atoms. Like MOR, the crystal lattice is orthorhombic. The length of the base vectors a, b, c is 20.07\AA , 19.92\AA and 13.42\AA respectively. MFI has the Pnma 62 space group, of which the operation are presented in Table 3b. In MFI, there are 12 unique T-sites present, and each T-site has a multiplicity of 8.

B.3 Dataset

The generated datasets contain 4992 MOR structures and 3296 MFI structures. In Figure 7, the distributions of the heat of adsorption for both datasets is visualized. It can be seen that for high heat of adsorption values (mainly for MFI), relatively few examples are present in the datasets. As such, it is likely that both models trained on the random and generalization data split will perform worse for heat of adsorption values in this range.

C Additional Results

C.1 Random Data Split

In addition to the figure presented in the paper, we also provide the data efficiency plot for the MSE for MOR and MFI in Figure 8. For both MOR and MFI, the plots are similar to the MAE plots in Figure 5, with the main difference being the scale on the y-axis.

C.2 Generalization Data Split

For the generalization task, we carried out the same experiments as with the random train/test split.

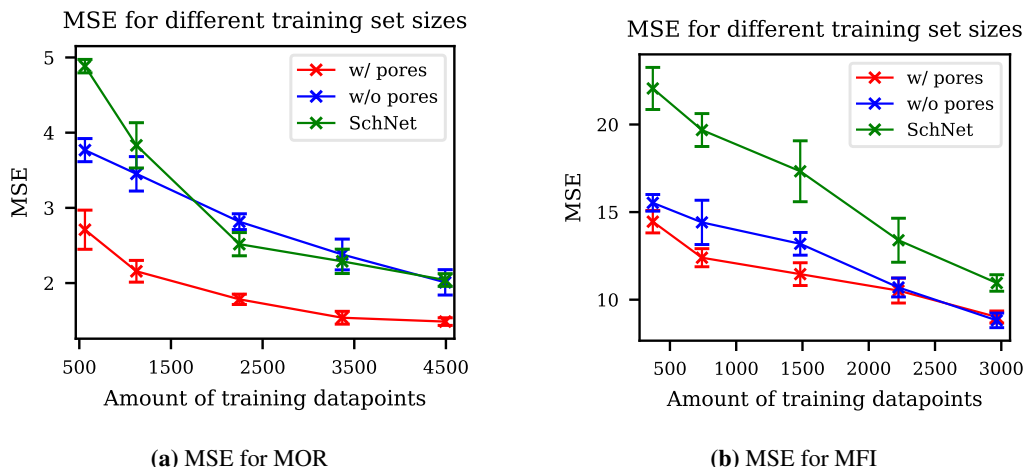


Figure 8: Data efficiency measured with the MSE on test set with different amounts of training data (random split).

As can be seen in Figure 9, the model for MOR still performs decently when having to generalize, while the model for MFI seems to struggle with higher heat of adsorption samples. This can also be seen in Table 2, where most models for MFI have a high MSE, indicating that they are making relatively large errors. We believe that the MFI models struggle to generalize due to a combination of the more complex structure of the material, as well as relatively few examples with high heat of adsorption values.

In Figure 10, the data efficiency for the generalization task is visualized. For MOR, we see that compared to the random train/test split, our model without pores seems to have a worse data efficiency than both SchNet and our model with pores. For MFI, we see that our model with and without pores have comparable performances. For the full dataset however, SchNet and the model without pores both seem to overfit, leading to an increased prediction error.

While the models perform worse on the generalization task, we believe that for the use case of predicting properties of materials this generally will not be an issue. When creating a training set, the data can be generated such that it covers a large portion of the data domain. As such, these models will mainly need to learn to interpolate between samples rather than extrapolate, a task for which we have shown that the model can obtain a good performance.

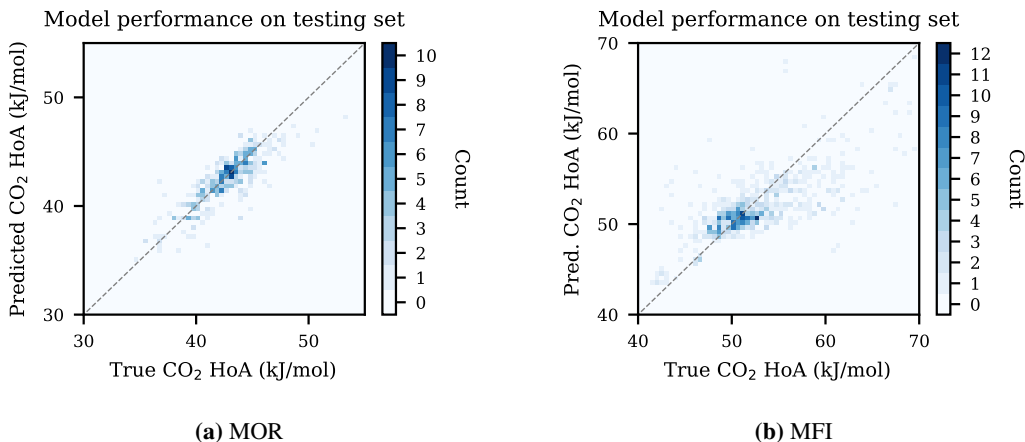


Figure 9: Predicted heat of adsorption plotted against the true heat of adsorption for the generalization train/test split. The best performing model with pores on the test set was used for MOR and MFI.

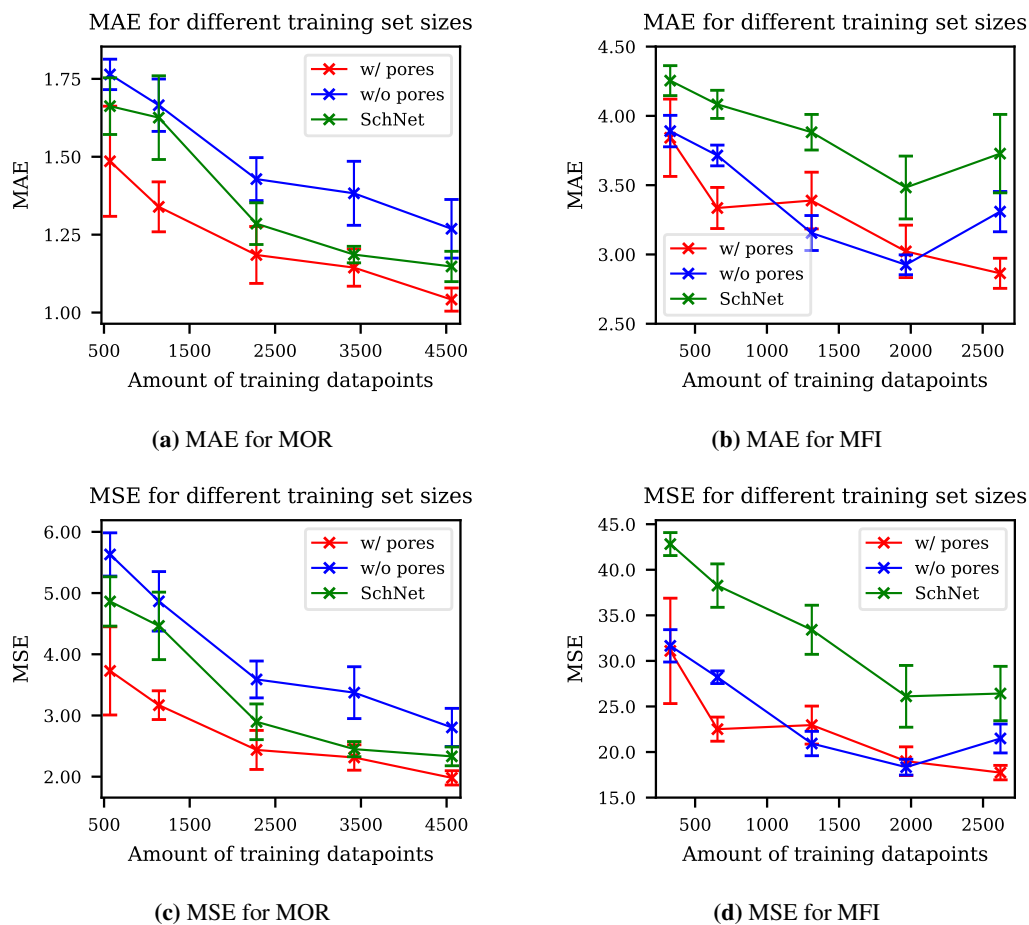


Figure 10: Data efficiency measured with the MAE and MSE on test set with different amounts of training data (generalization split).